PHYSICAL REVIEW E **92**, 032203 (2015)

Numerical approach to frictional fingers

Jon Alm Eriksen,[1,2,*] Renaud Toussaint,[1,2] Knut Jørgen Måløy,[1] Eirik Flekkøy,[1] and Bjørnar Sandnes[3]
[1]*Department of Physics, University of Oslo, P.O. Box 1048 Blindern, N-0316 Oslo, Norway*
[2]*Institut de Physique du Globe de Strasbourg, University of Strasbourg/EOST, CNRS, 5 rue Descartes, F-67084 Strasbourg Cedex, France*
[3]*College of Engineering, Swansea University, Bay Campus, Swansea SA1 8EN, United Kingdom*
(Received 2 May 2015; published 28 September 2015)

Experiments on confined two-phase flow systems, involving air and a dense suspension, have revealed a diverse set of flow morphologies. As the air displaces the suspension, the beads that make up the suspension can accumulate along the interface. The dynamics can generate "frictional fingers" of air coated by densely packed grains. We present here a simplified model for the dynamics together with a new numerical strategy for simulating the frictional finger behavior. The model is based on the yield stress criterion of the interface. The discretization scheme allows for simulating a larger range of structures than previous approaches. We further make theoretical predictions for the characteristic width associated with the frictional fingers, based on the yield stress criterion, and compare these to experimental results. The agreement between theory and experiments validates our model and allows us to estimate the unknown parameter in the yield stress criterion, which we use in the simulations.

DOI: 10.1103/PhysRevE.92.032203 PACS number(s): 45.70.Vn, 47.56.+r

I. INTRODUCTION

Petroleum reservoirs, aquifers, and geological formations are often highly fractured. Flows of gas, oil, groundwater, and magma tend to concentrate in the confined spaces of these fractures, as they have a much higher permeability than the porous matrix they are embedded in [1]. The permeable pathways can be of benefit to engineered processes; artificial stimulation of reservoirs by hydraulic fracturing is increasingly common as a means of increasing the production rate of low-permeability hydrocarbon reservoirs [2,3]. In other cases, high-permeability fractures pose a problem, as they contribute to increased groundwater contamination transport, leakage of buried radioactive wastes [1,4,5], and escape of sequestered carbon dioxide from geologic storage sites [6,7].

Flows in fractures and fractured media are difficult to characterize and predict, and this is especially so for multiphase flows, where interactions at interfaces between gas, liquid, or granular phases contribute to the fluid dynamics. Typically, when one fluid displaces another in a confined space, fluid instabilities and inherent disorder in the confining geometry result in an emerging patterning of the flow and a nontrivial mixing of the two fluids. Many of these flow phenomena, with applications to flow in fracture planes, have been studied in the idealized geometry of a Hele-Shaw cell. Examples includes viscous fingering in porous media [8–10] arising from the Saffman-Taylor instability [11,12], destabilized viscous fingers in suspensions [13], capillary fingering in a porous matrix [14–17], and the transition to fracturing [18,19]. Similar phenomena have also been observed with a single fluid displacing deformable porous media in Hele-Shaw cells [20–24].

We investigate here a two-phase flow phenomenon in a Hele-Shaw cell, where granular particles are suspended in the receding liquid phase. This system is known to display a rich set of flow morphologies as an immiscible fluid displaces the liquid granular mixture [25], for example, labyrinth patterns [26,27] and bubble structures [19,28]. In particular, we study the frictional finger formation, which develops as a layer of granular material accumulates at the fluid interface.

These finger structures are distinct from viscous fingers in several ways. First, the fingers are a result of static frictional forces in a local accumulated region of grains adjacent to the interface, rather than the global viscous pressure properties of the fluid phases. The frictional fingers develop in the quasistatic limit, where we can neglect the viscous forces. Second, unlike viscous fingers in porous media, which are known to display a fractal interface geometry [8,9,29,30], for frictional fingers we can identify a characteristic length, the finger width. While crossover behavior from frictional to viscous fingers has been observed as the driving rate is increased [19], we focus here on the quasistatic limit where static frictional forces dominate.

We present a new numerical scheme to simulate the frictional finger structures. This scheme builds on the strategy for simulating the labyrinth structures in [26] and [27] and contains crucial improvements for simulating fingers when the width of the accumulated layer of beads is comparable to the radius of curvature of the interface. We also present experimental results together with a theoretical model for the dynamics and predictions for how the characteristic finger width varies with the parameters. The theoretical comparison to experimental results validates our understanding and fixes a parameter used in the simulation.

In order to set the stage for the numerical scheme, in Sec. II we describe the details of the experimental system that we want to simulate. We present our theoretical model in Sec. III, and we describe the numerical scheme in detail in Sec. IV. In Sec. V, we present a derivation for the characteristic finger width and compare this to both the experimental and the numerical results. We, finally, sum up our findings in Sec. VI.

II. THE EXPERIMENT

A. Setup

Consider a Hele-Shaw cell, constructed as a rectangular channel, 20 cm wide, 30 cm long, and with a gap of

---

[*] jon.alm.eriksen@gmail.com

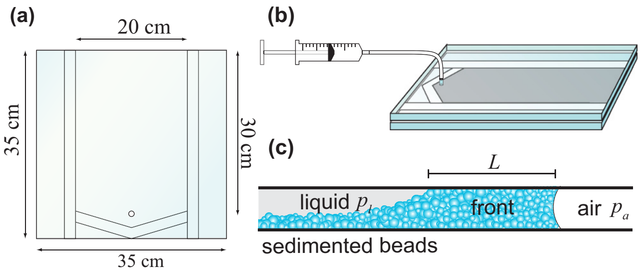

FIG. 1. (Color online) Experimental setup. (a) Hele-Shaw cell dimensions. (b) The system is fixed horizontally, filled with a fluid and sedimented beads, and driven either by air injection or by withdrawal of the liquid through a syringe pump connected at the nozzle at the sealed short side channel. (c) The advancing gas phase accumulates a front of grains.

$h = 0.5$ mm [Figs. 1(a) and 1(b)], filled with a suspension composed of a fluid mixture of glycerol and water along with glass beads [Fig. 1(c)]. The Hele-Shaw cell is fixed horizontally. The viscous fluid is a water-glycerol solution, 50% by volume. The viscosity of the liquid ensures that the beads are suspended during the filling of the cell, such that the beads are almost uniformly distributed in the cell plane. The beads are polydisperse, with a mean diameter of 75 μm [Fig. 2(a)], and are characterized by low granular friction [Fig. 2(b)] due to the almost-spherical shape of the grains [Fig. 2(c)]. The densities of the glass beads and the liquid are, respectively, $\rho_g = 2.4\ \mathrm{g/cm^3}$ and $\rho_l = 1.13\ \mathrm{g/cm^3}$. The density contrast, $\Delta\rho = \rho_b - \rho_l = 1.27\ \mathrm{g/cm^3}$, makes the beads sediment out of the liquid mixture and form a layer of granular material on the bottom plate of the Hele-Shaw cell, with a packing fraction which corresponds to a random loose packing fraction of spheres. The average thickness of this layer, relative to the gap of the cell, is referred to as the normalized filling fraction ϕ. The Hele-Shaw cell is sealed along the long sides and one of the short sides. The other short side is open to air at the ambient pressure.

The system is driven in one of two ways, which leads to the same dynamics in the range of parameters we consider. Either air is injected into the cell through an inlet nozzle located on the sealed short side or liquid is sucked out from the same nozzle and the air enters the cell from the open short side. A syringe pump (Aladdin WPI) is used in both cases. The driving rate varies in the range 0.01–0.03 ml/min. In the case of air injection, the syringe pump contains an air reservoir of 15 ml at atmospheric pressure, at the start of the experiment.

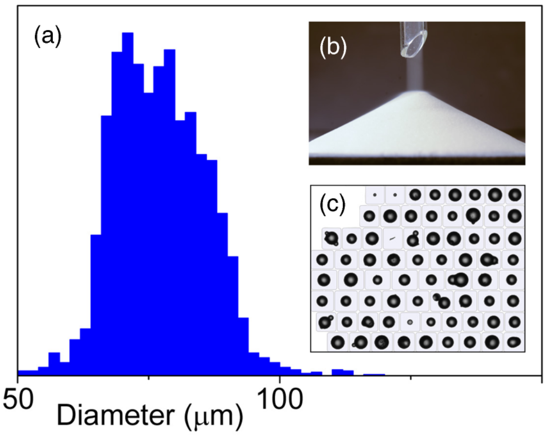

FIG. 2. (Color online) (a) Bead size distribution. (b) Cone of granular material poured through a funnel; angle of repose, ≈ 27°C. Microscopy images of beads (Malvern; Morphology G3) show thir approximately spherical shape.

B. Experimental results

As the air phase displaces the mixture, the interface bulldozes up the beads from the sedimented region, such that the beads accumulate along the air-liquid interface and fill the whole cell gap in a region adjacent to the interface. We refer to the region of accumulated beads as the *front* [see Fig. 1(c)]. After a short transient initial period, the entire interface develops a well-defined front. In the subsequent evolution, only a small section of the interface moves at any given time. The motion consists of stick-slip-like increments as the air phase fills an ever-increasing volume of the cell. The motion is always directed towards the liquid phase. A moving section of the interface tends to continue its motion over many consecutive stick-slip events, before it eventually stops and the motion continues at another section of the interface.

The friction from the accumulating front renders the advancing interface unstable, and the air phase develops fingerlike structures. The fingers have a characteristic width which emerges as a result of a balance between the interfacial tension and the friction of the front [19,26,27]. We refer to the pattern forming process as “frictional fingering,” to highlight the frictional component which distinguishes the patterning from viscous fingers resulting from the Saffman-Taylor instability [11]. Figure 3 shows a series of images taken at 2-h time intervals illustrating the pattern formation. The fingers branch out and grow in an isotropic, random fashion. Where two fingers meet or grow side by side, their fronts combine, and the motion of the interfaces stagnates. The fingers are prevented from merging by the beads in the front, and the gas phase thus constitutes a loopless, simply connected cluster, as does the residual granular-fluid phase. In the case of air injection, the evolution continues until a finger breaks through the outer boundary. In the case of liquid drainage, the evolution continues until the air phase reaches the inlet of the syringe pump. The final pattern of branching fingers is open, with pockets of undisturbed settled granular suspension of varying sizes left behind. Figure 4 shows a closeup showing the air fingers surrounded by a dark front of accumulated grains.

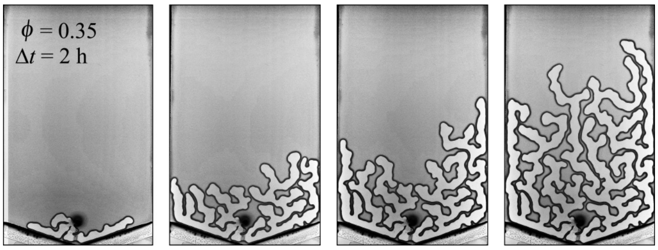

FIG. 3. The pattern formation process is documented over a 10-h period, with 2-h intervals between the individual images. Air is injected through the inlet at the bottom side. The cell is 20×30 cm.

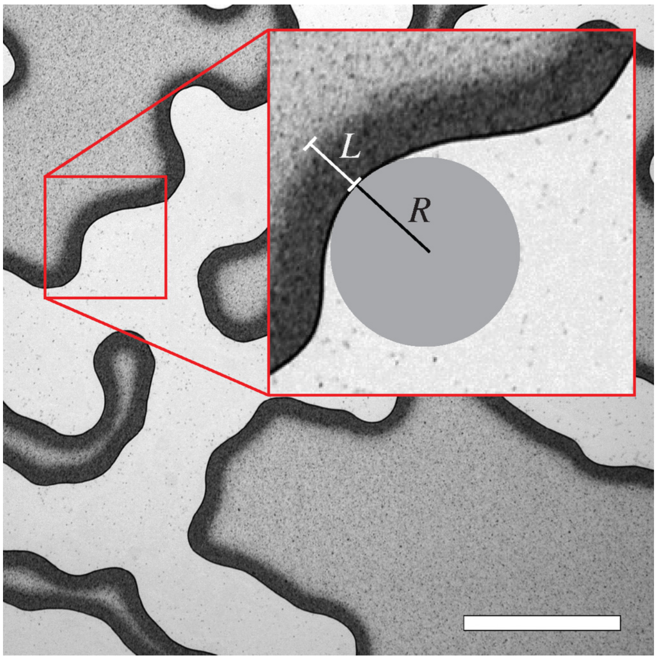

FIG. 4. (Color online) Closeup of the frictional finger pattern where the compacted front is visible as the dark band surrounding the air fingers. Inset: The front thickness L and the radius of curvature R, which are local parameters along the interface. The scale bar is 20 mm long.

As we increase ϕ, we observe a gradual decrease in the characteristic finger width, as shown in Fig. 5.

III. THEORETICAL MODEL

A. Stresses at the interface

It is instructive to make an order-of-magnitude estimate of the capillary number for the system, $\mathrm{Ca} = \mu V/\gamma$, where μ is the viscosity, V is the typical velocity and γ is the surface tension. The typical velocity of the finger growth, when averaged over many stick-slip cycles, can be estimated from the compression rate, $q = 0.01$–0.03 ml/min. Assuming that the width, w, of a moving section is $w \simeq 1$ cm, we have $V = q/(hw) \simeq 10^{-4}$ m/s. For the water-glycerol mixture we have that $\mu \simeq 6$ mPa s, and $\gamma = 60$ mN/m, which makes $\mathrm{Ca} \simeq 10^{-5}$. The small capillary number tells us that we can neglect the viscous pressure drop in the fluids; the relevant physics is confined to the interface.

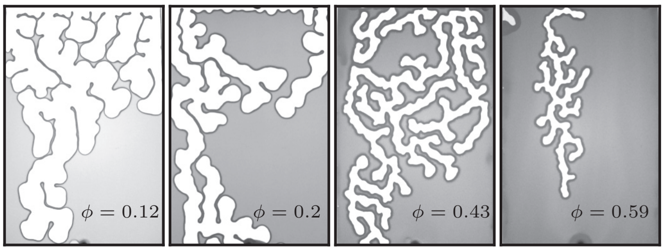

FIG. 5. Finger formation for increasing values of the filling fraction ϕ. Liquid is drained from the bottom side. The cell is 20 × 30 cm.

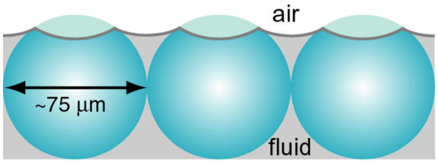

FIG. 6. (Color online) Sketch of the menisci around the beads at the air-liquid interface. The beads are wetting, resulting in concave menisci in the interspace between the beads.

The front can be characterized by a thickness, L, at any point along the mobile parts of the interface, i.e. the parts of the interface which have not yet stagnated due to the presence of a neighboring finger. This thickness is defined as the shortest distance from the air-liquid interface, through the accumulated beads, to a point where the beads no longer fill the whole cell gap [Fig. 1(c)].

The beads are wetting and the interface consists of concave menisci between the layer of beads closest to the air phase at the length scale of a bead diameter, as sketched in Fig. 6. The large-scale interface along the air side of the front region appears smooth, however, and we can assign a signed, in-plane curvature (κ) to every point along the interface, averaged over a number of neighboring beads. We define the curvature to be positive when the radius of curvature, $R = 1/|\kappa|$, can be drawn into the air phase (Fig. 4). The out-of-plane curvature component of the smoothed interface ($\kappa_\perp$) is constant along the interface.

We neglect the hydrostatic pressure difference over the height of the cell gap, and we approximate both the air pressure, p_a, and the liquid pressure, p_l, as uniform in their respective phases. The capillary pressure over the menisci between the beads is

$$\Delta p = p_a - p_l. \tag{1}$$

In the sticking state, the capillary pressure grows steadily. In the case of air injection, the air pressure increases due to the compression. In the case of fluid withdrawal, the liquid pressure decreases. We assign a capillary pressure threshold to every point along the interface, above which the nearby front gets mobilized and advances a small step towards the liquid; i.e., a slip event occurs.

This threshold depends on two effects. First, as the capillary pressure increases, the air-liquid menisci advances a small distance into the interspace between the beads, and the pull on the beads in the direction perpendicular to the smooth, large-scale interface is increased. This induces an effective stress, σ_e, on the bead packing normal to the averaged interface. Once this solid stress grows above the yield threshold of the bead packing, $\sigma_e > \sigma_Y$, the static packing breaks and the corresponding section of the front slides. This yield threshold is a local property of the mobile parts of the front, and in the subsequent discussion we approximate it by a linearly increasing function of the front thickness, L.

Second, when the front slips and moves a small step towards the fluid phase, the interface deforms and the surface energy changes. We assume that the changes in the total air-liquid surface, as the menisci advances into the interspace between the beads during the sticking state, is negligible.

The total surface energy of the air-liquid interface is, under this assumption, insensitive to the fluctuations in the capillary pressure during the intermittent dynamics of the interface. The surface energy scales with the number of menisci along the interface and, therefore, with the apparent area of the smoothed interface. We assign an effective surface tension, γ, to the smoothed interface, and the effective force which opposes an increase in surface area can be expressed according to Young's law as $\gamma(\kappa + \kappa_\perp)$. Note that the effective surface tension may deviate from the value of the surface tension of the liquid mixture. We do not, however, need its numerical value in the simulations described in the next section.

The threshold criterion for a slip of a section of the interface is given by

$$\Delta p > \gamma(\kappa + \kappa_\perp) + \sigma_Y(L). \tag{2}$$

The next moving section of the interface is identified by having local parameters κ and L, which minimize the right-hand side of Eq. (2). Note that $\kappa_\perp$ is constant along the interface and plays no role in the identification.

During a slip, new beads from the sedimented region accumulate at the front. The interface deforms, which alters the curvature κ. The interface may increase or decrease depending on the curvature, and the combined effect of deformation of the interface and the accumulation of new beads will change the local value of L. The menisci between the beads will retract, and the solid stress relaxes. A new static configuration of beads is formed and the motion stops. The interface evolves in a series of such stick-slip events.

Note that the capillary pressure over the menisci, Δp, at mobile regions of the interface remains well below the capillary pressure threshold for the interface to penetrate into the bead packing. The interface drags the beads along.

B. Approximating the yield stress

The effective stress, σ_e, is carried from frictional contacts along the Hele-Shaw cell boundaries to the interface, predominantly via force chains in the bead packing. The exact yield threshold, σ_Y, of a section of the interface depends on the bead configuration in the front region associated with the interface section. We approximate the yield stress as the sum of a discrete set of consecutive force bearing arc chains, in the direction perpendicular to the interface, each contributing with an average tangential stress along each boundary plate, $\sigma_\xi/2$. The total force per unit area opposing the motion and transmitted from the two boundaries is therefore σ_ξ. These chains have an associated length, ξ, in the direction through the front, and their number corresponds to L/ξ. We have

$$\sigma_Y = \sigma_\xi L/\xi. \tag{3}$$

The yield stress is thereby approximated as an increasing function of the front thickness.

Note that the linear L dependence of the yield stress can also be viewed as a linear approximation of a more complicated $\sigma_Y(L)$. Previous papers [26,27,31,32] have modeled $\sigma_Y(L)$ by use of the Janssen effect [33], i.e., that the shear stress at the plate boundaries is proportional to the normal stress in the direction perpendicular to the interface, which results in a yield stress which grows exponentially with L. Reference [31] also discusses how the curvature of the interface affects the bead stress. These models do, however, include extra unknown parameters which are hard to measure experimentally. We estimate the only unknown parameter for the simulations, i.e., $\gamma\xi/\sigma_\xi$, by experimental comparison to theoretical predictions in Sec. V. We further show that the linear approximation is in agreement with the experiments for the ranges of parameters considered here.

By combining Eqs. (2) and (3), we can write the slip criterion as

$$\Delta p > \gamma\kappa + \sigma_\xi L/\xi, \tag{4}$$

where we ignore the constant contribution of $\kappa_\perp$.

IV. SIMULATION

A. Numerical representation

We reproduce the behavior observed in the experiments by numerical simulations. The numerical approach is to represent the interface by a chain of nodes. Each node, i, contains information about its coordinates, (x_i,y_i), and its nearest neighbors, $i \pm 1$. The beads are represented by a two-dimensional bead concentration field, f, discretized into grid cells, $f_{n,m}$. The front is identified as all the grid cells of the bead concentration field with unit value, $f_{m,n} = 1$. The grid cells in the region which represents the sedimented layer of beads take the value of the initial filling fraction, $f_{n,m} = \phi$. All the grid cells in the interior regions of the chain, i.e., the region corresponding to the air phase, are ignored. The discretization is illustrated in Fig. 7.

We need to identify a front thickness, L_i, for every mobile node. We do this by identifying a *link* to a cell in the bead concentration field with a cell value of < 1; i.e., the cells which represent the sedimented region. This link is defined by the cell which has the minimum distance from the cell center to the node coordinates. The link thereby establishes a connection between the node index i and the field indices m and n, at the outer boundary of the front, and the length between the node and the cell center of the link cell defines L_i. Note that the direction towards the link cell which defines the front thickness may deviate from the direction perpendicular to the interface.

We also need to define a reasonable criterion for deciding when a node is stagnant. We do this by identifying a set of candidate cells to every node. These candidate cells are limited to a circular sector centered around the node position, spanned symmetrically by an angle of β, around the direction perpendicular to the interface [see the green region in Fig. 7(b)]. The radius of the circle sector, $L_{\max}$, serves as a cutoff length and needs to be set to a value much greater than the expected front thickness of a moving segment but less than the finger width. In the following we use the experimentally observed finger half-width, $L_{\max} = \Lambda$ (see Fig. 11), and $\beta = 90^\circ$. If a link cannot be established within these candidate cells, i.e., all the candidate cells take unit values or are in the interior of the chain, the node is considered stagnant.

It is convenient to define an ideal node separation length δ, and we can use this length scale as a basis unit for the other length scales in the simulation. We set this length to $\delta =$

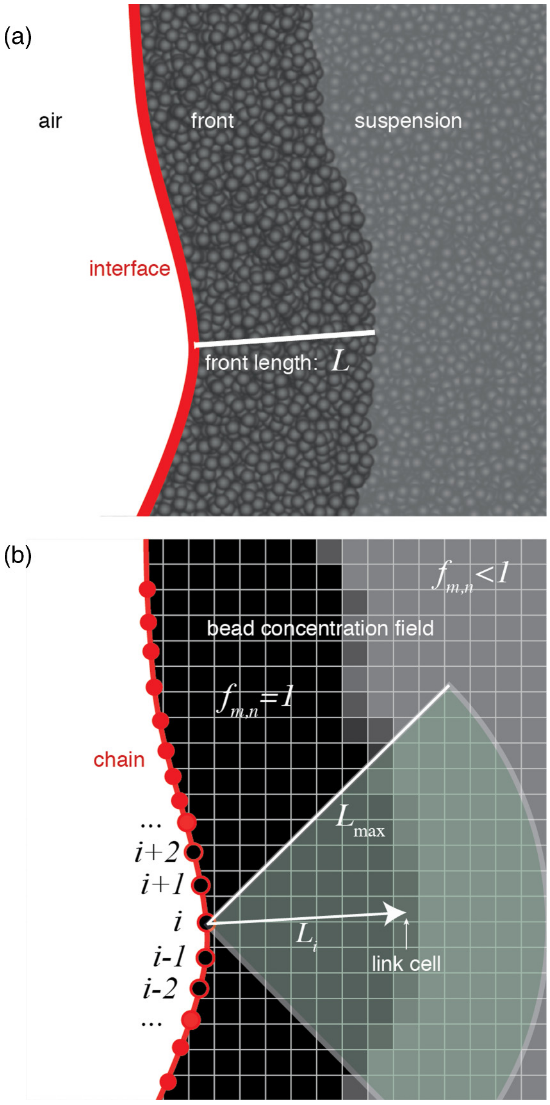

FIG. 7. (Color online) Discretization procedure. (a) Hele-Shaw cell seen from above. The air phase is on the left-hand side. Adjacent to the air interface is the front, which is an accumulated region of beads. We can assign a front thickness, L, at every mobile point along the interface. (b) The interface is discretized as a chain of nodes. The beads are discretized into a two-dimensional concentration field, which takes the value 1 in the front, and the initial filling fraction ϕ in the regions of not yet accumulated/sedimented beads. The size of the grid cells and the node spacing are exaggerated for the purposes of the illustration. L_i is the shortest distance from node i, through the accumulated regions, to a point in the bead field below 1. The grid-cell candidates are limited to the shaded circular section of 90°, centered around the direction perpendicular to the interface.

0.4 mm (i.e., a chain corresponding to an interface which spans the width of the Hele-Shaw cell is composed of approximately 500 nodes). Note that this length scale is slightly smaller than the Hele-Shaw cell gap, which is 0.5 mm. The grid-cell spacing of the bead concentration field, δ_{grid}, is set to $\delta_{\mathrm{grid}} = 2/3 \times \delta \simeq 0.27$ mm. Note that these lengths (δ and δ_{grid}) are both larger than the size of an individual grain (Fig. 2). The grid spacing of the bead concentration field will naturally limit the resolution of the front thickness. The size of δ may be adjusted to provide a better resolution. To mask the direction of the underlying grid structure, we need to modify the front thickness by an additional random number uniformly distributed in the interval $(-\delta_{\mathrm{grid}},\delta_{\mathrm{grid}})$, which corresponds to the resolution of the grid. The front thickness is, however, ill defined on this length scale; the random modification will not alter the large-scale behavior.

The curvature, κ_i, is estimated by calculating derivatives of a spline approximation of the interface. We use a two-dimensional B spline [34], which is parameterized by the piecewise linear approximation to the arc-length parameter. The first derivative of the spline at the position of the central node gives the unit tangent vector. The second derivative gives the curvature vector, which points in the direction perpendicular to the interface. The FITPACK library [34] is used to efficiently calculate the spline and its derivatives.

The curvature and the front thickness of the theoretical model relevant for the simulation are local to the interface, and we can assign a threshold value, Δp_T^i, to every node. By discretizing Eq. (4), we have that this threshold value is given by

$$\Delta p_T^i = \gamma\kappa_i + L_i\frac{\sigma_\xi}{\xi} = B\left(\frac{\xi\gamma}{\sigma_\xi}\kappa_i + L_i\right), \tag{5}$$

where B is a multiplicative constant. The node corresponding to the minimal value of the right-hand side will be insensitive to B. We use the numerical value of $\xi\gamma/\sigma_\xi = 0.0361\ \mathrm{cm}^2$. This value comes from the estimated by experimental observations of the characteristic length Λ, which we discuss in the next section (Fig. 11).

Before we go on describing the dynamics in the next subsection, we spend a couple of paragraphs justifying the discretization scheme we have described. Using a chain of nodes, i.e., Lagrangian tracer particles, to represent a moving interface, rather than, e.g., contours of an indicator field, has certain problematic aspects [35]. The accuracy and the stability of this chain representation are dependent on the node spacing, which will vary as some nodes moves together, while others separate. Redistribution and interpolation of nodes are therefore necessary to faithfully represent the interface, and we describe this in detail in the following subsection. We also have to make sure that the topology of the interface remains simple, in the sense that a node is not allowed to move in between others and thereby move into the interior of the interface. These are issues which are absent if the interface is represented as a contour. For our specific problem, however, the chain representation has a number of advantages, which outweighs the above-mentioned problems.

Only a small section of the total interface will move at any given time. Computation is therefore limited to a subset of easily identifiable active nodes. The chain representation permits us also to sort nodes by a lower bound for the threshold, which enables an efficient identification of the next moving node. The stress threshold of an inactive node, j, may change. This can happen if the displacement of active nodes adds mass to the region near the inactive node, such that L_j increases, or by the displacement of neighboring nodes which alters the curvature κ_j. The stress threshold of an inactive node, separated from the active nodes by at least the number of neighbors used to estimate the curvature, can, however, never decrease. We can, therefore, store a lower threshold bound for these nodes. The chain representation of the nodes is also convenient for calculating the area enclosed by the chain, as we can easily triangulate the enclosed domain.

B. Dynamics

We model the motion of the interface by iteratively moving a small segment of the chain. Moving multiple nodes, rather than a single one, is necessary to keep the interface, and its curvature, smooth. A time step constitutes the motion of a set of neighboring nodes, in the direction towards the suspension. As the air flux is constant, we can infer the true time from the displaced area.

In the following, we need to make some arbitrary choices regarding the number of moving nodes, etc. The numerical results seem to be insensitive to the specific rules, as long as the size of the displacement of the nodes at every time step is sufficiently small and the curvature at the boundary nodes and its neighbors (see Fig. 8) varies sufficiently smoothly.

The moving segment is limited to three neighbors on each side (seven nodes in total), and all of them need to be mobile. The center node, i, of the moving segment is, at every time step, identified by the minimum of the pressure threshold, Eq. (5),

$$i = \operatorname{argmin}_j \Delta p_T^j. \tag{6}$$

The new position of the interface is approximated by calculating a spline function, as shown in Fig. 8. This spline is calculated on the basis of the two nonmoving next neighboring nodes on each side of the seven moving nodes and the point lying a distance $\delta_{\text{move}} = 0.1\delta$ from the previous coordinates of the central node, in the perpendicular direction outwards from the chain. To calculate the spline, we also need the arc-length parameter for the interface *after* the movement. To estimate this, we use the arc length of the segment before it moves and modify it with a factor, s, corresponding to the stretch, or contraction, in accordance with the mean curvature along the moving segment. If a circle with radius R expands, such that $R \to R + \delta_{\text{move}}$, the circumference, C, is modified by a factor $C \to C(1 + \delta_{\text{move}}/R)$. By analogy, we approximate the expansion by

$$s = 1 + \bar{\kappa}\delta, \tag{7}$$

where $\bar{\kappa}$ is the average curvature of the all the moving nodes. The positions of the new nodes are set by equidistantly distributing the moving node coordinates along this new spline. Note that the width of the moving section is fixed: seven nodes move at each time step. This width is smaller than the typical width of a slipping section event in the experiments, which can correspond to the finger width. When we iterate many time steps, we recover the behavior of the experiments.

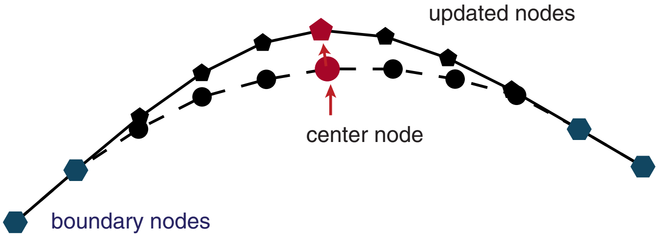

FIG. 8. (Color online) Schematic of the moving segment. Seven nodes are moving. The old configuration is represented by circles on the dashed line; the new configuration, by pentagons on the solid line. The spline which determines the updated positions is based on the two neighboring nodes on each side of the interval (hexagons) and the center node moved a distance δ_{move} in the direction normal to the chain. The positions of the new nodes are distributed along the spline function. Dimensions in the figure are exaggerated.

At every time step, we also need to accumulate beads in the concentration field, to ensure mass conservation. We can easily triangulate the displaced area, by considering the coordinates of the moving nodes, before and after the displacement. By calculating the area of the triangulation, we can associate an amount of displaced beads with every moving node. The beads corresponding to this area will be added to its link grid cell. If the total of the new beads and the existing bead mass at the closest grid cell exceeds 1, the grid-cell value is set to 1 and the residual mass is added to the next link grid cell. This is repeated until either all the mass is displaced or no link is found among the node's candidate grid cells, in which case the node is considered stagnant for the rest of the simulation. When two front segments merge their nodes will naturally turn stagnant. It is therefore not necessary to control for overlapping segments.

Before we start a new time step, we use the spline to interpolate the chain. We calculate the total arc length, S, of the moving segment between the first nonmoving boundary nodes on both sides of the moving interval. We get the ideal number of nodes, N_{nodes}, to fill in between the boundary nodes by $N_{\text{nodes}} = \text{round}(S/\delta) - 1$. If this number differs from 7 (the original number of moving nodes), we equidistantly redistribute N_{nodes} nodes along the spline, between the boundary nodes.

We can sum up the algorithm by the following procedure. At each time step we:

(1) Identify the next moving node by Eq. (6), and its neighbors.

(2) Estimate the spline function for the new configuration.

(3) Iteratively move each node, accumulating the bead concentration field according to the displaced area for every moved node.

(4) Add or subtract and redistribute nodes if necessary.

To induce some random behavior which results in the fingering pattern, we add a random perturbation to the bead concentration field. This random perturbation is limited by ±5% and is correlated over an $\simeq 50$-grid point, corresponding to the width of $\simeq 1$ cm. We generate this distribution by a bicubic interpolation of a field of uncorrelated variables, with 50 interpolated points between each uncorrelated value. This noise is needed to trigger the branching of the fingers.

A series of frames for the evolution of the finger structures generated by this numerical scheme is shown in Fig. 9. This numerical scheme differs from the one used in [27], to simulate labyrinth patterns in a similar system, in two important ways. First, a set of neighboring nodes, rather than a single one, is moved at every time step. This is done to assure that the curvature remains reasonably smooth and allows us to use several neighboring nodes (more than three) to approximate the derivatives of the path of the interface, which in turn is used to define the curvature and the perpendicular direction.

Second, the granular field is numerically represented as a two-dimensional field, rather than a local quantity which

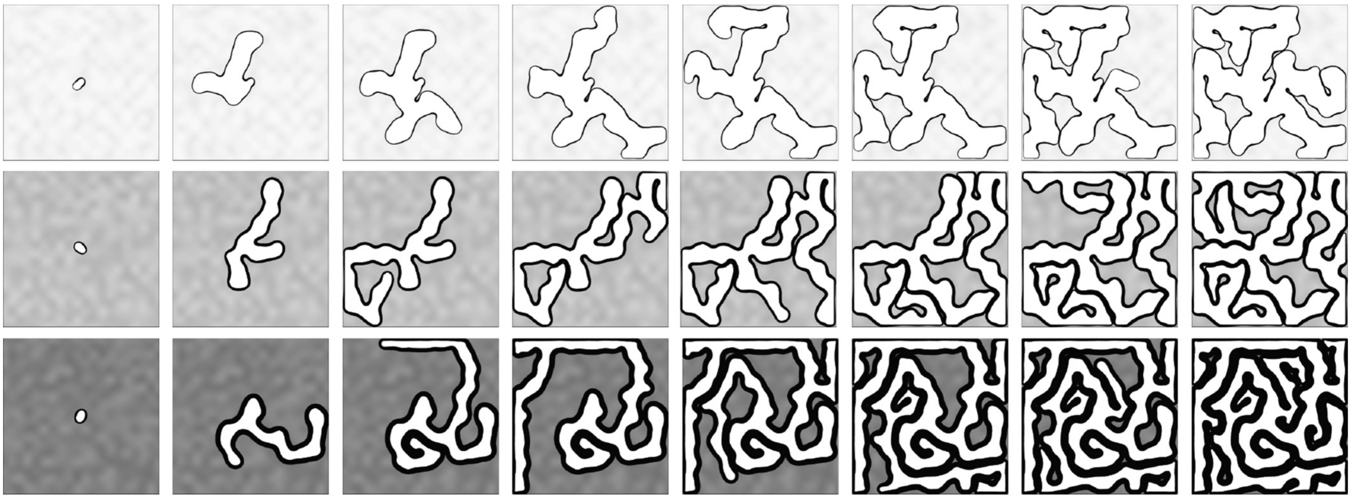

FIG. 9. Examples of the evolution of the numerical scheme with a central, circular injection point. The size of the geometry is 10 × 10 cm. Each row represents a time series of the evolution. Top row, $\phi = 0.1$; middle row, $\phi = 0.3$; and bottom row, $\phi = 0.5$. There is an additional noise field in the initial bead configuration, limited to $\phi \to \phi \pm 0.05$.

moves with the nodes of the interface. In the scheme presented in [27], each node contains a thickness vector in the direction perpendicular to the interface, whose length equals the front thickness. Each pair of neighboring nodes spans out a trapezoid, such that the corners correspond to the nodes' positions and the positions of the thickness vectors. The front is thereby effectively represented as a chain of trapezoids (see Fig. 7 in [27]). This scheme works fine as long as the node separation, i.e., the resolution, needed to simulate the structures is approximately equal to the front thickness. If the node separation is small compared to the length of the thickness vectors, small deformations of the chain could lead to large displacements of the thickness vectors, which again leads to large errors in the mass conservation of the front. Moreover, neighboring thickness vectors could cross, and the front representation would be completely unphysical. A small node separation compared to the front thickness is indeed needed in order to faithfully discretize the system at $\phi > 0.35$, i.e., beyond the results for labyrinth structures presented in Ref. [27]. This is needed for the application of simulation aligned fingers in a tilted Hele-Shaw cell [36].

V. THE CHARACTERISTIC LENGTH

Consider a steadily growing finger as shown in Fig. 10. The curvature is 0 at the sides of the finger and $1/R$ at the fingertip. Let L_t and L_s be the front thickness at the tip and at the side of the finger, respectively. In the quasistatic approximation, we have that the pressure threshold over the front at the side of the fingers equals that of the fingertip. By Eq. (4), we have

$$\frac{\sigma_\xi}{\xi} L_s = \frac{\gamma}{R} + \frac{\sigma_\xi}{\xi} L_t. \tag{8}$$

The frictional fingers can be characterized by a width, and we let Λ denote half this finger width as shown in Fig. 10. As the cell gap, h, is constant, we have that the air volume in the Hele-Shaw cell scales with the apparent area of the air phase as seen from above, A_{air}, and that the surface area of the interface scales with the apparent circumference, C, of the air-liquid interface. The ratio between the enclosed area and the circumference of the air phase, $\Lambda = A_{\text{air}}/C$, will on average correspond to half of the finger width and serves as a natural definition of a characteristic length.

Consider now a single finger which moves into the suspension. An increment of the displaced air volume, $h\delta A_{\text{air}}$, where δA_{air} is the increased area of the air phase, will be accompanied by an increased volume of the front $h\delta A_{\text{front}}$, due to the accumulation of new beads. Mass conservation gives that

$$\delta A_{\text{front}} = \frac{\phi}{1-\phi} \delta A_{\text{air}}. \tag{9}$$

The curvature (κ) varies smoothly along the interface and will take its maximum value at the fingertip. We can approximate a small section around the fingertip by a circular shape, with a radius, R, equal to the reciprocal of the maximum curvature. We assume that the finger moves in a steady

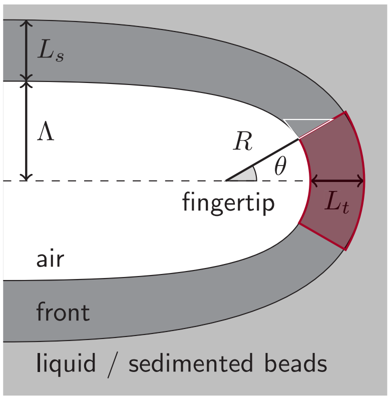

FIG. 10. (Color online) Schematic of a steadily growing finger. Λ is half the finger width, L_s is the front thickness at the sides of the finger, and L_t is the front thickness of the fingertip. The annulus section at the fingertip identifies a small region of the front at the fingertip, bounded by an angle θ. The maximum curvature of the fingertip is $\kappa = 1/R$.

state, such that the fingertip retains its shape during the evolution. The area element of the front of the fingertip can be approximated by a section of an annulus (Fig. 10). The area of this section is $A_{\text{front}} = \theta((R + L_t)^2 - R^2)$, where θ is a small angle which binds the section on both sides of the fingertip. A small variation of this element, with respect to θ and L_t, is given by

$$\delta A_{\text{front}} = 2\theta(R + L_t)\delta L_t + \left(2RL_t + L_t^2\right)\delta\theta. \tag{10}$$

When the tip of the finger moves forward by an infinitesimal distance, δx, the air volume associated with the front element increases by $\delta A_{\text{air}} = 2\theta R\delta x + O(\delta x^2)$. Note that the interface at θ moves a distance $\delta x \cos\theta$ in the direction normal to the interface (along the longest cathetus of the white triangle in Fig. 10), to retain the circular shape. This perpendicular displacement stretches the original section of the interface. The projection of the displacement onto the circular interface gives $R\delta\theta = \delta x \sin\theta \simeq \delta x\theta$ (along the shortest cathetus of the open white triangle in Fig. 10), where the latter approximation is valid when $\theta \ll 1$. When we combine this with Eqs. (9) and (10), we get

$$\left(1 + \frac{L_t}{R}\right)\frac{\delta L_t}{\delta x} = \frac{\phi}{1-\phi} - \frac{L_t}{R}\left(1 + \frac{L_t}{2R}\right). \tag{11}$$

At steady state, we have $\delta L_t/\delta x = 0$, which leads to the following condition at the fingertip:

$$\frac{L_t}{R} = \sqrt{\frac{1+\phi}{1-\phi}} - 1. \tag{12}$$

This expression provides a correction to Eq. (22) in Ref. [27], which reads $L_t/R = \phi/(1-\phi)$. Note that $\phi/(1-\phi) = \phi + \phi^2 + O(\phi^3)$, while an expansion of Eq. (12) reads $\phi + \phi^2/2 + O(\phi^3)$. By comparison, the new expression provides a correction in the second-order term in the ϕ expansion of the result.

We assume that a steadily growing finger will grow in a way which minimizes the threshold pressure. When we use Eq. (12) to eliminate $\kappa = 1/R$ in the pressure threshold for the fingertip [Eq. (4) evaluated at equality], we get

$$\Delta p = \frac{\gamma}{L_t}\left(\sqrt{\frac{1+\phi}{1-\phi}} - 1\right) + \frac{\sigma_\xi}{\xi}L_t. \tag{13}$$

Minimizing the right-hand side with respect to L_t gives

$$L_t = \sqrt{\frac{\gamma\xi}{\sigma_\xi}\left(\sqrt{\frac{1+\phi}{1-\phi}} - 1\right)}. \tag{14}$$

Mass conservation dictates that $L_s/\Lambda = \phi/(1-\phi)$. Using this with Eqs. (8), (12), and (14) gives

$$\Lambda = 2\sqrt{\frac{\gamma\xi}{\sigma_\xi}}\chi, \tag{15}$$

where we have introduced

$$\chi = \frac{1-\phi}{\phi}\sqrt{\sqrt{\frac{1+\phi}{1-\phi}} - 1} \tag{16}$$

to simplify the notation.

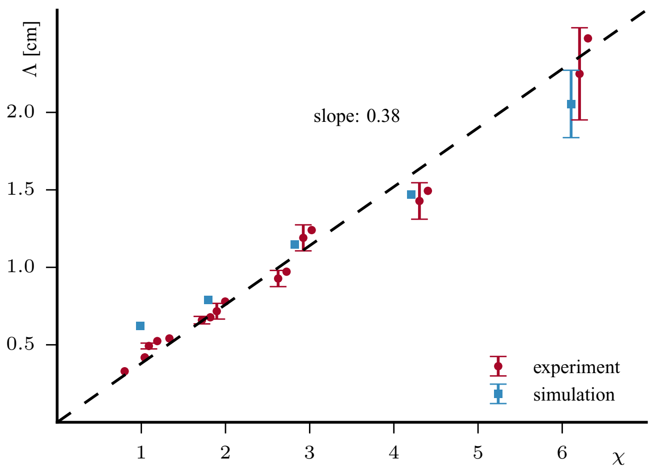

FIG. 11. (Color online) The characteristic length Λ is the ratio between the area of the finger structures and the finger structure circumference. Error bars correspond to one standard deviation; data points without error bars correspond to single observations. The dashed line corresponds to the best fit of the theoretical prediction in Eq. (15). The slope of 0.38 cm corresponds to the numerical value prefactor $2\sqrt{\gamma\xi/\sigma_\xi}$, which is used to infer the numerical value of $\xi\gamma/\sigma_\xi$.

This relationship is clearly seen when we plot the experimentally observed Λ versus χ (Fig. 11). We use the linear coefficient to estimate $\gamma\xi/\sigma_\xi = (0.38/2)^2 = 0.0361$ cm^2 in the simulation, which again gives consistent results for Λ calculated for the resulting patterns of the simulations (Fig. 11), although the results of the simulations overpredict Λ slightly for low values of χ, i.e., high values of ϕ. Note that if we expand χ in $\phi/(1-\phi)$, we have that $\chi \simeq \sqrt{(1-\phi)/\phi}$ to leading order.

A similar prediction for Λ can be made when a yield stress of the bead packing [$\sigma_Y(L)$] grows exponentially with L [27]. The good agreement among experiments, simulations, and theory (Fig. 11) validates the linear approximation [Eq. (3)] for the ranges of parameters we consider here.

VI. CONCLUSION

In conclusion, we have presented a new numerical scheme for simulating frictional fingers. The scheme discretizes the interface as a chain of nodes which is coupled to a two-dimensional mass field, needed to calculate the accumulated layer of beads along the interface. This numerical representation improves an earlier scheme [27] and enables us to simulate structures where the front thickness is large compared to the length scale at the details of the interface.

The dynamics is generated by a simplified threshold model based on the effective surface tension of the interface and the bead stress in the front [Eq. (4)]. The only free parameter in the model is inferred from the comparison of the experimentally observed finger width to the theoretically predicted value (Fig. 11). We successfully reproduce experimentally observed patterns (Figs. 9 and 11).

The branching behavior of the finger growth is triggered by noise in the system. In the experimental setup there are multiple sources of noise, e.g., fluctuations in the force chains through the front, which result in the static friction, variations in the static friction properties between the beads and the bounding glass plates, and variations in the height between the glass plates. The dominating source of noise in the simulation is the imposed fluctuations in the bead field. In addition, noise in the simulation arises from the discretization of the chain and the noise imposed on L_i, which is needed to mask the underlying grid. While the noise in the simulation is sufficient to generate patterns which share the same qualitative structures as the experimental result (compare Figs. 3, 5, and 9), exactly how the correlation of the different sources of noises affects the branching behavior remains an open question. This question lies outside the scope of this article, but we note that this might be studied by considering how the branching geometry is affected by the imposed correlation structure in the initial bead field.

Another line of future research is to use the discretization procedure to simulate bubble structures seen in the same experimental setup [19,28]. As discussed in Sec. IV B, the discretization scheme does not rely on a small front thickness relative to the radius of curvature, as previous approaches did [27]. The numerical representation described here can in principle represent the highly curved front segments along the interface of a bubble. Such a simulation would, however, need a dynamical rule more sophisticated than Eq. (4) to account for the bubble expansion.

ACKNOWLEDGMENTS

We thank Benjy Marks for discussions at various stages of the project. J.A.E. acknowledges support from the Research Council of Norway through CLIMIT Project No. 200041 and from Campus France through the Eiffel Grant. B.S. acknowledges support from EPSRC Grant No. EP/L013177/1. R.T., K.J., and E.G.F. acknowledges support from The European Union's Seventh Framework Programme for research, technological development, and demonstration under Grant Agreement No. 316889-ITN FlowTrans. R.T. also acknowledges support from the University of Oslo and Université de Strasbourg.

[1] M. Sahimi, *Flow and Transport in Porous Media and Fractured Rock: From Classical Methods to Modern Approaches*, 2nd ed. (Wiley-VCH Verlag, Weinheim, Germany, 2011).

[2] R. Vidic, S. Brantley, J. Vandenbossche, D. Yoxtheimer, and J. Abad, Science **340**, 1235009 (2013).

[3] T. Patzek, F. Male, and M. Marder, Proc. Natl. Acad. Sci. USA **110**, 19731 (2013).

[4] B. Berkowitz, Adv. Water Resour. **25**, 861884 (2002).

[5] C.-F. Tsang and I. Neretnieks, Rev. Geophys. **36**, 275 (1998).

[6] A. Cavanagh, Int. J. Greenh. Gas Con. **21**, 101 (2014).

[7] J. Song and D. Zhang, Environ. J. Sci. Tech. **47**, 9 (2013).

[8] K. J. Måløy, J. Feder, and T. Jøssang, Phys. Rev. Lett. **55**, 2688 (1985).

[9] J.-D. Chen and D. Wilkinson, Phys. Rev. Lett. **55**, 1892 (1985).

[10] G. M. Homsy, Annu. Rev. Fluid Mech. **19**, 271 (1987).

[11] P. G. Saffman and G. Taylor, Proc. R. Soc. London A: Math. Phys. Sci. **245**, 312 (1958).

[12] D. Bensimon, L. P. Kadanoff, S. Liang, B. I. Shraiman, and C. Tang, Rev. Mod. Phys. **58**, 977 (1986).

[13] C. Chevalier, A. Lindner, and E. Clement, Phys. Rev. Lett. **99**, 174501 (2007).

[14] R. Lenormand and C. Zarcone, Phys. Rev. Lett. **54**, 2226 (1985).

[15] R. Lenormand, E. Touboul, and C. Zarcone, J. Fluid Mech. **189**, 165 (1988).

[16] A. Birovljev, L. Furuberg, J. Feder, T. Jøssang, K. J. Måløy, and A. Aharony, Phys. Rev. Lett. **67**, 584 (1991).

[17] V. Frette, J. Feder, T. Jøssang, and P. Meakin, Phys. Rev. Lett. **68**, 3164 (1992).

[18] R. Holtzman, M. L. Szulczewski, and R. Juanes, Phys. Rev. Lett. **108**, 264504 (2012).

[19] B. Sandnes, E. G. Flekkøy, H. A. Knudsen, K. J. Måløy, and H. See, Nat. Commun. **2**, 288 (2011).

[20] E. Lemaire, Y. O. M. Abdelhaye, J. Larue, R. Benoit, P. Levitz, and H. van Damme, Fractals **1**, 968 (1993).

[21] Ø. Johnsen, R. Toussaint, K. J. Måløy, and E. G. Flekkøy, Phys. Rev. E **74**, 011301 (2006).

[22] X. Cheng, L. Xu, A. Patterson, H. M. Jaeger, and S. R. Nagel, Nature Phys. **4**, 234 (2008).

[23] M. J. Niebling, R. Toussaint, E. G. Flekkøy, and K. J. Måløy, Phys. Rev. E **86**, 061315 (2012).

[24] M. J. Niebling, R. Toussaint, E. G. Flekkøy, and K. J. Måløy, Rev. Cub. Fis. **29**, 1E66 (2012).

[25] B. Sandnes, E. G. Flekkøy, K. J. Måløy, and J. A. Eriksen, Rev. Cub. Fis. **29**, 1E23 (2012).

[26] B. Sandnes, H. A. Knudsen, K. J. Måløy, and E. G. Flekkøy, Phys. Rev. Lett. **99**, 038001 (2007).

[27] H. A. Knudsen, B. Sandnes, E. G. Flekkøy, and K. J. Måløy, Phys. Rev. E **77**, 021301 (2008).

[28] B. Sandnes, E. Flekkøy, and K. Måløy, Eur. Phys. J. Spe. Topics **204**, 19 (2012).

[29] G. Løvoll, Y. Méheust, R. Toussaint, J. Schmittbuhl, and K. J. Måløy, Phys. Rev. E **70**, 026301 (2004).

[30] R. Toussaint, G. Løvoll, Y. Méheust, K. J. Måløy, and J. Schmittbuhl, Europhys. Lett. **71**, 583 (2005).

[31] J. A. Eriksen, B. Marks, B. Sandnes, and R. Toussaint, Phys. Rev. E **91**, 052204 (2015).

[32] B. Marks, B. Sandnes, G. Dumazer, J. A. Eriksen, and K. J. Måløy, Front. Phys. **3**, 41 (2015).

[33] H. A. Jannsen, Z. D. Vereines Deutscher Inginieure **39**, 1045 (1895).

[34] P. Dierckx, *Curve and Surface Fitting with Splines* (Oxford University Press, Oxford, UK, 1995).

[35] J. Sethian, *Level Set Methods and Fast Marching Methods Evolving Interfaces in Computational Geometry, Fluid Mechanics, Computer Vision, and Materials Science* (Cambridge University Press, Cambridge, UK, 1999).

[36] J. A. Eriksen, R. Toussaint, E. G. Flekkøy, K. J. Måløy, and B. Sandnes (unpublished).